

## ORIGINAL RESEARCH ARTICLE

Hierarchical Bayesian model selection for  
three-dimensional-printed cementitious  
materialsFelipe Guerrero\*, Albert R. Ortiz, Peter Thomson, and Daniel GomezSchool of Civil and Geomatics Engineering, Faculty of Engineering, Universidad del Valle, Cali,  
Valle del Cauca, Colombia

## Abstract

Three-dimensional (3D) concrete printing presents significant challenges in accurately modeling mechanical behavior due to the anisotropy induced by layer-by-layer deposition and variability in inter-filament bonding. This study introduces a hierarchical Bayesian framework for selecting and calibrating constitutive models in 3D-printed cementitious materials. Three candidate models—parabolic (Model 1), Carreira–Chu (Model 2), and plastic-damage (Model 3)—were assessed using uniaxial compression data from (i) soil–cement pastes with calcium carbonate additions (0–10%), (ii) cast and 3D-printed mortars, and (iii) 3D-printed concrete tested under perpendicular and parallel loading orientations. Bayesian inference combined with information criteria (Watanabe–Akaike Information Criterion and leave-one-out cross-validation) enabled objective model selection and uncertainty quantification. The Carreira–Chu model consistently outperformed alternatives for homogeneous systems (soil–cement and mortars), while the plastic-damage model best represented anisotropic responses in printed concrete loaded parallel to the deposition direction. Experimental findings indicate a 44% decrease in elastic modulus with 10% calcium carbonate, a 9.1% increase in compressive strength for printed versus cast mortars (8.36 vs. 7.66 MPa), and a 21% strength gain in concrete loaded parallel versus perpendicular to the deposition direction, despite a 40% reduction in stiffness. The proposed hierarchical Bayesian approach provides probabilistic estimates of constitutive parameters (compressive strength, elastic modulus, and characteristic strain) and data-driven guidance for selecting suitable models for additive manufacturing of cementitious materials, enhancing the reliability of structural simulations of 3D-printed elements.

## \*Corresponding author:

Felipe Guerrero  
(felipe.guerrero@correounivalle.  
edu.co)

**Citation:** Guerrero F, Ortiz AR, Thomson P, Gomez D. Hierarchical Bayesian model selection for three-dimensional-printed cementitious materials. *Mater Sci Add Manuf.* 2026;5(2):025460109.  
doi: 10.36922/MSAM025460109

**Received:** November 13, 2025**Revised:** December 20, 2025**Accepted:** December 24, 2025**Published online:** April 2, 2026

**Copyright:** © 2026 Author(s).  
This is an Open-Access article distributed under the terms of the Creative Commons Attribution License, permitting distribution, and reproduction in any medium, provided the original work is properly cited.

**Publisher's Note:** AccScience Publishing remains neutral with regard to jurisdictional claims in published maps and institutional affiliations.

**Keywords:** Three-dimensional-printed concrete; Cementitious materials; Bayesian inference; Model calibration

## 1. Introduction

Three-dimensional (3D) concrete printing represents a pivotal technology in the digitalization and automation of the construction industry, enabling the fabrication of structures with complex geometries while optimizing material usage.<sup>1</sup> 3D concrete printing offers advantages over conventional concrete, including greater geometric freedom, reduced waste, decreased reliance on labor, and the potential for faster and

more cost-effective construction.<sup>2</sup> Its ability to fabricate complex structural elements without the need for costly formwork is undoubtedly one of its most relevant features.<sup>3</sup>

However, 3D concrete printing introduces significant challenges in characterizing and modeling its mechanical properties. The structural performance of printed elements is affected by anisotropy generated by the layer-by-layer deposition process and variability in inter-filament adhesion, as noted by van Zijl *et al.*<sup>4</sup> The rheological performance of printable materials has been identified as a critical factor in determining printability, as material behavior during printing directly influences the success of printed structures.<sup>5</sup> Ensuring the quality and safety of printed structures requires an understanding of the mechanical behavior of the material in both its fresh and hardened states.<sup>6</sup> The fresh state influences printability and dimensional stability, while the hardened state determines the material's strength and durability.<sup>7</sup>

This study implements a Bayesian inference-based approach to characterize 3D-printed materials, addressing these challenges. We analyze three types of materials: (i) soil–cement pastes with varying proportions of calcium carbonate ( $\text{CaCO}_3$ ), (ii) a concrete mix designed for 3D printing, and (iii) mortars with natural sand. Compression tests on both molded and 3D-printed samples clearly indicate that three constitutive models are necessary to describe the stress–strain relationship.

Bayesian inference was used to estimate the parameters of each model and quantify their uncertainty. We used model selection criteria, such as Watanabe–Akaike Information Criterion (WAIC) and leave-one-out (LOO) cross-validation, to identify the model that best represents the mechanical behavior of the evaluated materials. This approach provides a more robust characterization of 3D-printed materials, ensuring their reliability for use in structural simulations and the design of construction elements.

The main contributions of this work are as follows. First, we applied a hierarchical Bayesian framework to quantify uncertainty in constitutive model parameters. Second, we conducted a comparative analysis using WAIC and LOO to select the most appropriate model for each material. Finally, we provide recommendations for the use of the selected models in structural simulations of 3D-printed elements.

## 2. Materials and methods

This section outlines the experimental framework and analytical methodologies employed in this study. Section 2.1 details the materials characterization through

uniaxial compression testing, while Section 2.2 presents the constitutive models evaluated. Section 2.3 describes the hierarchical Bayesian framework used for model calibration and selection.

### 2.1. Materials and experimental characterization

This section presents the uniaxial compression test data used for calibrating constitutive models. Three types of materials were considered, all intended for potential application in 3D concrete printing: soil–cement paste with  $\text{CaCO}_3$  addition, mortar with natural sand, and 3D-printed concrete.

It is worth noting that current test methods and standards used for the characterization of construction materials and conventional structures are not fully suitable for direct application to cementitious materials used in 3D printing.<sup>8</sup> Therefore, while different specimen geometries were adopted for each material type (soil–cement, mortar, and concrete), the experimental design focused on model selection within each material group. This approach enabled the evaluation of specific parameters: the effect of  $\text{CaCO}_3$  additions in pastes, the manufacturing process (cast vs. printed) in mortars, and anisotropy in printed concrete.

All tests were conducted using a Tinius Olsen (United States) H50KS universal testing machine under displacement-controlled conditions. In accordance with American Society for Testing and Materials C109 guidelines, a testing speed of 1 mm/min was used for all compressive strength ( $f_c$ ) tests. The corresponding stress–strain curves were recorded for each case.

#### 2.1.1. Soil–cement paste

The term soil–cement paste refers to a mixture composed of soil and cement, without the inclusion of sand or other aggregates. In this study, the soil used corresponds to a natural soil collected in Villa Rica, Cauca (Colombia). The specimens were prepared in the form of cubes with 20 mm sides and cured for 28 days.

Three levels of  $\text{CaCO}_3$  addition were evaluated: 0%, 5%, and 10% by mass relative to the dry soil content. For each level, four specimens were tested to examine the effect of this additive on the mechanical response of the paste. Stress–strain curves were computed from the recorded load and displacement data, as shown in Figure 1A.

#### 2.1.2. Mortar with natural sand

Mortar specimens made with natural sand were tested, with a focus on the influence of the fabrication method. Cubic samples with 38 mm sides were prepared using two approaches: conventional casting and 3D printing. For

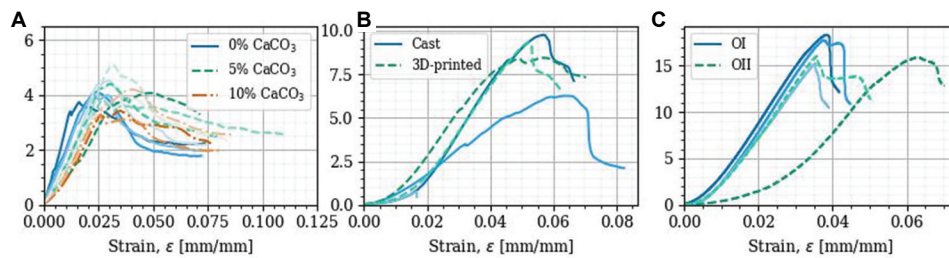


**Figure 1.** Stress–strain curves. (A) Soil–cement paste with varying calcium carbonate ( $\text{CaCO}_3$ ) content (0%, 5%, 10%). (B) Mortar with natural sand (cast vs. three-dimensional [3D]-printed). (C) 3D-printed concrete under perpendicular (Orientation I) and parallel (OII) loading orientations

each fabrication method, three specimens were tested after 28 days of curing.

The 3D printing process was performed using a desktop printer (Creality Ender-3, Shenzhen Creality 3D Technology Co., Ltd., China) with a build volume of  $220 \times 220 \times 250$  mm. The printer was equipped with a piston-based extrusion system, consisting of a cylindrical chamber and a plunger, with a material capacity of  $600 \text{ cm}^3$ . The resulting stress–strain curves are shown in Figure 1B.

### 2.1.3. Three-dimensional-printed concrete

The experimental data correspond to uniaxial compression tests performed on concrete cubes measuring 50 mm per side, which were extracted by cutting from a larger 3D-printed element. The specimens were cured under standard laboratory conditions before testing.

To examine directional behavior in printed concrete, two loading orientations were considered. In Orientation I (OI), the load was applied perpendicular to the printing direction, i.e., across the filament layers. In Orientation II (OII), the load was applied parallel to the direction in which the material was extruded. For each orientation, three specimens were tested under displacement-controlled conditions. Axial strain was recorded through strain gauges adhered to the specimen surfaces. The corresponding stress–strain curves are shown in Figure 1C.

### 2.2. Constitutive models and approaches

The development of printable materials for concrete additive manufacturing highlights the urgent need to investigate and evaluate innovative methods that enhance interlayer adhesion under large-scale printing conditions and in real-world environments.<sup>9</sup> A key aspect of this development is optimizing key properties of fresh concrete, such as flowability and cohesion, to ensure the structural integrity and printing stability. This technique boasts significant advantages over conventional methods, offering greater geometric freedom without the need for costly formwork.<sup>7,10</sup>

The quality of 3D-printed structures depends on the material performance in both its fresh and hardened states.<sup>16</sup> While the fresh state requires precise control of rheological properties and hydration to avoid printing failures, the hardened state must guarantee sufficient stiffness and strength, which are influenced by printing conditions, layer thickness, interlayer bonding, and porosity.<sup>7</sup>

In its hardened state, 3D-printed concrete exhibits anisotropic mechanical behavior, where properties vary according to the loading direction. Paul *et al.*<sup>11</sup> examined cubic and prismatic specimens on the third day of curing, cutting them from printed elements while accounting for the print orientation, as illustrated in Figure 2A. Their study, which conducted compression and flexural tests in accordance with the British Standard adopted from European Norm 196-1:2016, showed that printed samples had lower mechanical properties than molded ones, confirming anisotropic behavior. Similarly, Ding *et al.*<sup>12</sup> defined a coordinate system to characterize this anisotropy, taking into account the filament direction and the print plane, which is shown in Figure 2B.

Further studies have expanded on this understanding. Kaliyavaradhan *et al.*<sup>13</sup> compared printed and molded specimens, while Chougan *et al.*<sup>14</sup> evaluated prismatic samples at 7 days of curing, highlighting the effect of admixtures. Tay *et al.*<sup>9</sup> examined the influence of process parameters, including printing speed and layer thickness. To determine properties such as the elastic modulus ( $E$ ) and Poisson's ratio, Kruger and Westhuizen<sup>15</sup> determined that core extraction orientation significantly affects the mechanical properties. Le *et al.*<sup>16</sup> and Feng *et al.*<sup>17</sup> analyzed tensile and flexural properties, showing that anisotropy is closely tied to filament orientation and interlayer adhesion.

Table 1 summarizes the most common experimental protocols that have been documented in the literature.<sup>18</sup> A preponderance of studies has demonstrated that mechanical anisotropy is an inherent property of the 3D printing process. This finding necessitates the implementation of characterization protocols that explicitly consider loading

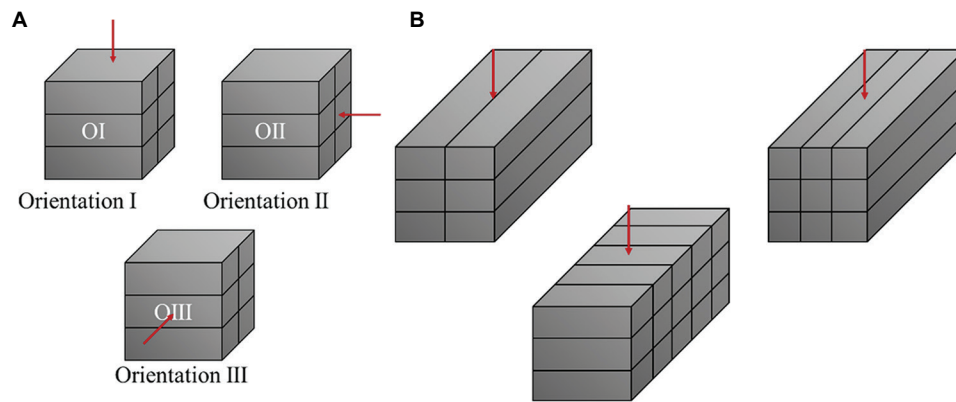


**Figure 2.** Loading configurations for mechanical testing of three-dimensional-printed cementitious elements. (A) Layer-dependent compression orientations for cubes. (B) Print-direction schemes for flexure in prisms

**Table 1. Hardened-state mechanical properties and test methods**

Property	Test	Description	References
Compressive strength	Compression test	Measurement of the capacity of 3D-printed concrete layers to resist compressive load	ASTM C39/C39M-18e1
Flexural strength	Flexural strength test	Measurement of the capacity of 3D-printed concrete layers to resist bending load	ASTM C78/C78M-18, ASTM C293/C293M-19, ASTM C348/C348M-19, ASTM C1583-19
Anisotropy	Compression, flexural, and tension tests	Application of load parallel and perpendicular to the printed layers	14,16,19-22
Tensile stress	Uniaxial tension test	Measurement of deformation and applied force on the specimen	ASTM C496/C496M-17

Note: Data adapted from Riaz *et al.*<sup>18</sup>.

Abbreviations: 3D: Three-dimensional; ASTM: American Society for Testing and Materials.

directions relative to print orientation for structural applications.

The mechanical response of 3D-printed cementitious materials has been modeled using a wide range of formulations. Rheological models such as the Bingham approach<sup>23,24</sup> describe the viscoplastic behavior of fresh concrete during extrusion, while for hardened materials, porosity-based<sup>25,26</sup> and orthotropic formulations<sup>7,27</sup> have been proposed to capture anisotropic elastic or damage behavior under multiaxial loading. However, these approaches mainly address flow or anisotropy under complex stress states, which are beyond the scope of this study.

Here, we focused on the compressive response of hardened materials under uniaxial loading, selecting three constitutive models for Bayesian calibration and comparison: a parabolic model, the Carreira–Chu model, and a plastic-damage model.

## 2.2.1. Model 1: Parabolic model for cementitious powder-based materials

The model proposed by Feng *et al.*<sup>17</sup> describes the stress–strain behavior of 3D-printed materials using a parabolic formulation Equation (1):

$$\sigma = \frac{f_0 - E_0 \epsilon_u}{\epsilon_u^2} \epsilon^2 + E_0 \quad (1)$$

In this model,  $f_c$  denotes the peak compressive strength,  $E_c$  is the initial elastic modulus, and  $\epsilon_u$  corresponds to the ultimate strain. The parameter ( $\epsilon_u$ ) must satisfy the condition in Equation (2):

$$\epsilon_u \geq \frac{2f_0}{E_0} \quad (2)$$

The parabolic expression captures an initially linear response that becomes progressively smoother as the applied stress increases, without exhibiting a clearly defined horizontal segment in the stress–strain curve.

## 2.2.2. Model 2: Carreira–Chu model

The Carreira–Chu model is one of the most widely used and cited empirical models for describing the stress–strain curve of 3D-printed concretes under uniaxial compression.<sup>28,29</sup> This model captures the entire stress–strain response, including the post-peak softening. As a proper rational fraction model, its formulation is shown in Equation (3):

$$\frac{\sigma}{f_c} = \frac{\epsilon}{\epsilon_0} \star \frac{n}{n-1 + \left(\frac{\epsilon}{\epsilon_0}\right)^n} \quad (3)$$

where the parameter  $n$  relates to the initial elastic modulus ( $E_c$ ) and maximum strength ( $f_c$ ) through Equation (4):

$$n = \frac{E_c \epsilon_0}{E_c \epsilon_0 - f_c} \quad (4)$$

With  $\epsilon_0$  being the strain at peak stress.

### 2.2.3. Model 3: Plastic-damage model for concrete

The plastic-damage model originally developed by Saenz<sup>30</sup> has been adapted to characterize the nonlinear behavior of 3D-printed concrete under compressive loading.<sup>31</sup> The constitutive formulation describing the stress-strain relationship is given by Equation (5):

$$\sigma = \frac{E_0 \epsilon_c}{1 + \left[ \left( \frac{E_0 \epsilon_p}{\sigma_p} \right) - 2 \right] \left( \frac{\epsilon_c}{\epsilon_p} \right) + \left( \frac{\epsilon_c}{\epsilon_p} \right)^2} \quad (5)$$

Where  $(\sigma_p)$  and  $(\epsilon_p)$  are the peak stress and the corresponding strain, respectively. Although tensile behavior is not addressed in this study, the damage model proposed by Hordijk<sup>32</sup> has been applied in previous works<sup>31</sup> to describe the tensile softening of cementitious materials.

Each of these models provides a distinct formulation of the stress-strain response, from smooth parabolic hardening (Model 1) to rational fraction softening (Model 2) and damage-based behavior (Model 3). These models were calibrated through hierarchical Bayesian inference, as detailed in Section 2.3, to evaluate their ability to reproduce experimental compressive data from the tested materials.

### 2.3. Hierarchical Bayesian methodology for model selection

Bayesian inference is a probabilistic framework used to update hypotheses about a model as new evidence becomes available. Using Bayes' Theorem, the probability of a set of parameters  $\theta$ , given a dataset  $D$ , is expressed as Equation (6):

$$P(\theta|D) = \frac{P(D|\theta) \cdot P(\theta)}{P(D)} \quad (6)$$

This formulation allows the incorporation of prior knowledge about parameters through the prior distribution  $P(\theta)$ , and it adjusts this hypothesis based on observed data, resulting in the posterior distribution  $P(\theta|D)$ . In problems involving limited or noisy data, this approach is

particularly useful, as it provides a flexible mechanism to quantify uncertainty.

Hierarchical Bayesian inference extends this framework by introducing structured models with multiple levels of complexity. In such models, lower-level parameters for individual samples (e.g.,  $E_p, f_{c,i}$  for specimen  $i$ ) are treated as drawn from common higher-level population distributions (e.g.,  $\mu_E, \mu_{f_c}$ ), which are also estimated from data. This hierarchical structure is well-suited for experimental data organized into subpopulations sharing common statistical properties.

In this study, a two-level hierarchical Bayesian framework was implemented to calibrate three selected constitutive models: a parabolic model (Model 1), the Carreira-Chu model (Model 2), and a plastic-damage model (Model 3). For each material (paste, mortar, and 3D-printed concrete), distinct prior distributions and hierarchical structures were defined, tailored to the characteristics of each experimental dataset. Model selection was carried out using the WAIC<sup>33</sup> and LOO cross-validation,<sup>34</sup> both of which quantify out-of-sample predictive performance while penalizing model complexity. Since the analysis was conducted within a Bayesian framework, the performance of the different constitutive models was not evaluated using traditional metrics, such as the coefficient of determination or root mean square error. Instead, predictive capability was evaluated by computing the expected log predictive density (ELPD) using both WAIC and LOO. These metrics were specifically chosen to compare the models' out-of-sample prediction accuracy, providing a robust basis for selection that accounts for uncertainty and model complexity.

All materials followed the same two-level structure: Level 1 (Specimens):  $\theta_i \sim N(\mu_\theta, \sigma_\theta)$ , Level 2 (Population):  $\mu_\theta \sim \pi(\mu)$ ,  $\sigma_\theta \sim \pi(\sigma)$  where  $\theta_i$  represents the constitutive parameters (e.g., strength  $f$ , modulus  $E$ , strain  $\epsilon$ ) of the  $i$ -th specimen, and  $\pi(\cdot)$  refers to the prior distributions defined for each parameter. The hierarchical organization of the model is summarized schematically in Figure 3, illustrating the relationships between specimen-level parameters, population-level hyperparameters, and the observed data used for Bayesian calibration.

The prior distributions for the constitutive parameters were defined based on material type, sample size, and available prior knowledge regarding mechanical behavior. For all materials, independent priors were used for  $f_c$ ,  $E$ , and characteristic strain ( $\epsilon$ ). Uniform distributions were selected for population means ( $\mu_\theta$ ) to impose minimal assumptions within physically plausible ranges, while half-normal distributions were used for standard deviations

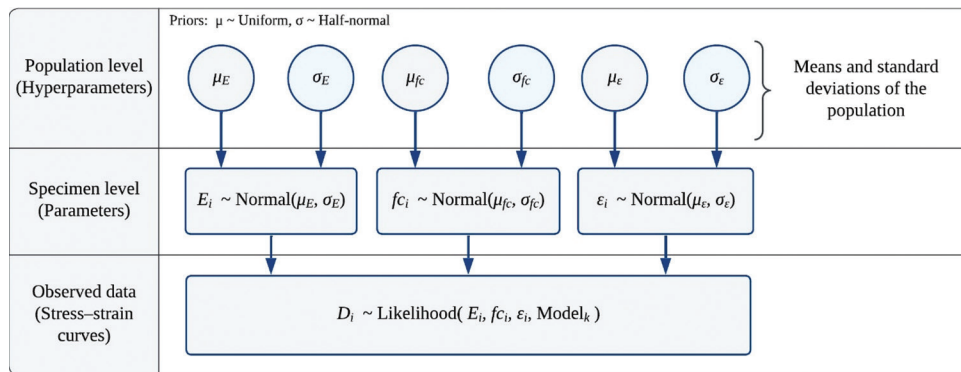


**Figure 3.** Schematic representation of the two-level hierarchical Bayesian framework used for model calibration and selection

( $\sigma_\theta$ ) to regularize variability. Table 2 summarizes the distribution types and ranges for each parameter.

For Model 1, the parabolic formulation requires  $\mu_\epsilon \leq 2 \mu_{f_0}/\mu_{E_0}$  to maintain convexity. This condition was enforced via a logarithmic penalty function added to the model's log-likelihood. In the case of 3D-printed concrete, wider priors were specified to account for the greater uncertainty arising from the reduced sample size ( $n = 3$ ).

### 2.3.1. Computational implementation

The Bayesian inference process was implemented using PyMC v5.15,<sup>35</sup> employing the No-U-Turn Sampler algorithm. For each model and material combination, four independent Markov chains were executed in parallel, each with 2,000 iterations, including 1,000 warm-up steps for tuning. Convergence diagnostics were based on the potential scale reduction factor ( $\hat{R}$ ),<sup>36,37</sup> defined as Equation (7):

$$\hat{R} = \sqrt{\frac{\text{Var}^+(\theta y)}{W}} \quad (7)$$

Where  $\text{Var}^+(\theta y)$  is the marginal posterior variance and  $W$  is the within-chain variance. All parameters satisfied the convergence criterion  $\hat{R} < 1.1$ . Additionally, the effective sample size for each parameter exceeded 400, ensuring reliable posterior estimation.

## 3. Results

This section presents the results of the Bayesian calibration and model selection processes for each material. The results are organized as follows: the posterior parameter distributions are first analyzed to assess uncertainty and variability in the mechanical response; then, the optimal constitutive model is selected using WAIC and LOO criteria; finally, the estimated parameters are summarized.

The Bayesian approach enables robust inference even with a small number of experimental observations, which

**Table 2.** Prior distributions defined for each constitutive parameter by the material

Material	Parameter	Population means	Standard deviations
Paste (soil–cement)	$f_c$	Uniform (2.5, 7.0)	Half-normal (0.5)
	$E$	Uniform (100, 400)	Half-normal (80)
	$\epsilon$	Uniform (0.005, 0.012)	Half-normal (0.001)
Mortar	$f_c$	Uniform (5.0, 11.0)	Half-normal ( $0.2 \mu_t$ )
	$E$	Uniform (80, 300)	Half-normal ( $0.2 \mu_E$ )
	$\epsilon$	Uniform (0.003, 0.1)	Half-normal ( $0.2 \mu_\epsilon$ )
Three-dimensional-printed concrete	$f_c$	Uniform (10, 40)	Half-normal (5.0)
	$E$	Uniform (500, 2000)	Half-normal (150)
	$\epsilon$	Uniform (0.002, 0.015)	Half-normal (0.002)

Abbreviations:  $\epsilon$ : Characteristic strain;  $E$ : Elastic modulus;  $f_c$ : Compressive strength.

in this case were limited to four specimens per condition for soil–cement paste, and two to three for mortar and printed concrete. This methodological choice allows not only point estimates but full probabilistic descriptions of each parameter.

The highest density interval (HDI) is reported to describe the most credible parameter ranges, typically covering 90% of the posterior probability mass. This complements the maximum a posteriori (MAP) estimates and the residual parameter  $\sigma$ , which quantifies the variability due to both experimental noise and model uncertainty.

### 3.1. Soil–cement paste

The posterior distributions of the mechanical parameters for the soil–cement paste are shown in Figure 4, where the parameters  $E$ , peak strain,  $f_c$ , and residual variability ( $\sigma$ ) were compared across three candidate models (rows) and three  $\text{CaCO}_3$  contents (colors). The Carreira–Chu model (Model 2) exhibited the narrowest posterior distributions

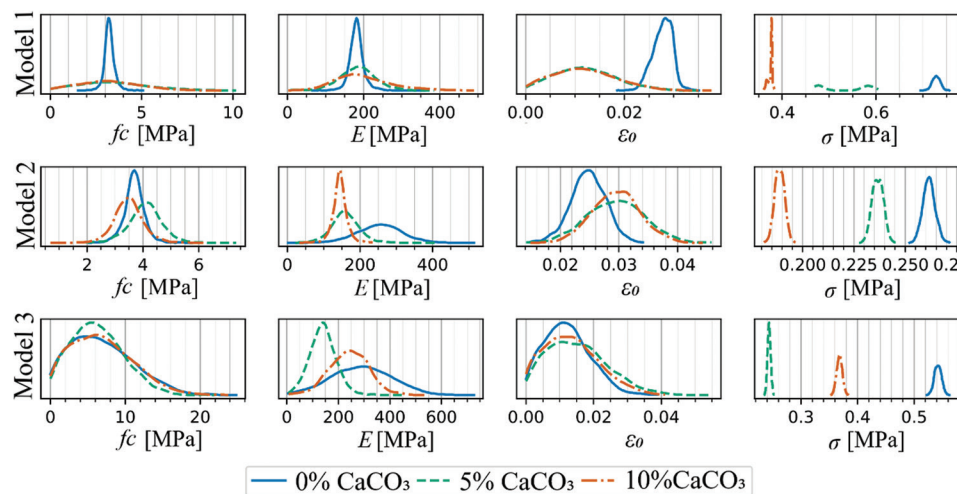


**Figure 4.** Posterior distributions for soil–cement paste parameters. Rows: Models 1–3. Columns: compressive strength ( $f_c$ ), elastic modulus ( $E$ ), peak strain ( $\epsilon_o$ ), and residual variability ( $\sigma$ ). Colors denote calcium carbonate ( $\text{CaCO}_3$ ) content: 0% (blue), 5% (green), 10% (orange)

for  $E$  and  $f_c$ , indicating more precise parameter estimation across all additive levels.

Model selection results in Figure 5 confirm that Model 2 consistently outperformed the alternatives at all calcium carbonate contents. The ELPD difference between Model 2 and the next-best model exceeded 2,000, particularly at higher additive contents, demonstrating its superior predictive capability.

Table 3 summarizes the posterior statistics for the parameters of Model 2. The  $E$  decreased progressively with higher  $\text{CaCO}_3$  content, from an MAP of 256.9 MPa at 0%  $\text{CaCO}_3$  to 142.7 MPa at 10%, corresponding to a 44% reduction. The  $f_c$  peaked at 4.0 MPa for 5%  $\text{CaCO}_3$  and decreased to 3.4 MPa at 10%, suggesting that moderate additive levels provided optimal mechanical performance. The  $\sigma$  decreased with higher  $\text{CaCO}_3$  content, from 0.262 MPa at 0% to 0.189 MPa at 10%, indicating improved model fit despite reduced stiffness. Overall, the Carreira–Chu model (Model 2) provided the most accurate and stable representation of the compressive response across all additive levels, effectively capturing the nonlinear transition from elasticity to plasticity in soil–cement paste.

### 3.2. Mortar with natural sand

The posterior distributions for the mortar specimens, shown in Figure 6, reveal differences between cast and 3D-printed samples. In cast mortar, Model 2 produced concentrated posterior distributions, particularly for  $\epsilon_o$ . In contrast, the 3D-printed mortar exhibited broader posteriors for  $f_c$ , indicating greater uncertainty in strength associated with the additive manufacturing process.

**Table 3. Comprehensive parameter estimates for Model 2 (soil–cement paste)**

Parameter	% $\text{CaCO}_3$	Mean	SD	5% HDI	95% HDI	MAP
$E$ (MPa)	0	253.42	60.76	148.64	347.67	256.89
	5	158.06	39.66	94.32	221.39	160.12
	10	142.88	20.29	111.23	173.01	142.67
$\epsilon_o$	0	0.025	0.003	0.02	0.03	0.0246
	5	0.029	0.005	0.021	0.037	0.029
	10	0.029	0.004	0.023	0.036	0.0299
$f_c$ (MPa)	0	3.702	0.385	3.107	4.318	3.713
	5	4.095	0.621	3.113	5.064	3.998
	10	3.497	0.538	2.671	4.406	3.447
$\sigma$ (MPa)	0	0.262	0.003	0.257	0.267	0.2617
	5	0.237	0.003	0.232	0.241	0.2377
	10	0.189	0.002	0.185	0.193	0.1887

Abbreviations:  $\epsilon_o$ : Peak strain;  $\sigma$ : Residual parameter;  $E$ : Elastic modulus;  $f_c$ : Compressive strength;  $\text{CaCO}_3$ : Calcium carbonate; HDI: Highest density interval; MAP: Maximum a posteriori; SD: Standard deviation.

Model selection results in Figure 7 indicate that Model 2 remains the optimal choice for both cast and printed specimens. The ELPD values were  $-3,826.05 \pm 45.65$  for the cast mortar and  $-3,411.95 \pm 32.57$  for the 3D-printed mortar.

The parameter estimates in Table 4 indicate that 3D printing resulted in an increase in  $f_c$  and a slight improvement in stiffness compared to casting. Specifically, the MAP of  $f_c$  was 8.35 MPa for the printed mortars and 7.56 MPa for the cast ones, corresponding to an increase of approximately

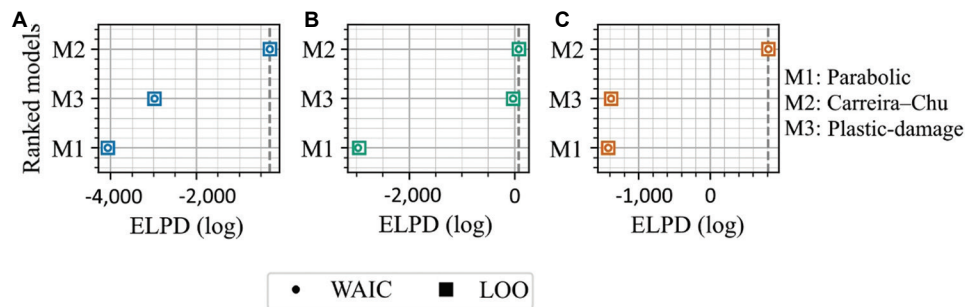


**Figure 5.** Model comparison for soil-cement paste via WAIC/LOO. Higher ELPD indicates superior predictive performance. (A) 0% CaCO<sub>3</sub>, (B) 5% CaCO<sub>3</sub>, (C) 10% CaCO<sub>3</sub>. Abbreviations: CaCO<sub>3</sub>: Calcium carbonate; ELPD: Expected log predictive density; LOO: Leave-one-out; WAIC: Watanabe–Akaike Information Criterion

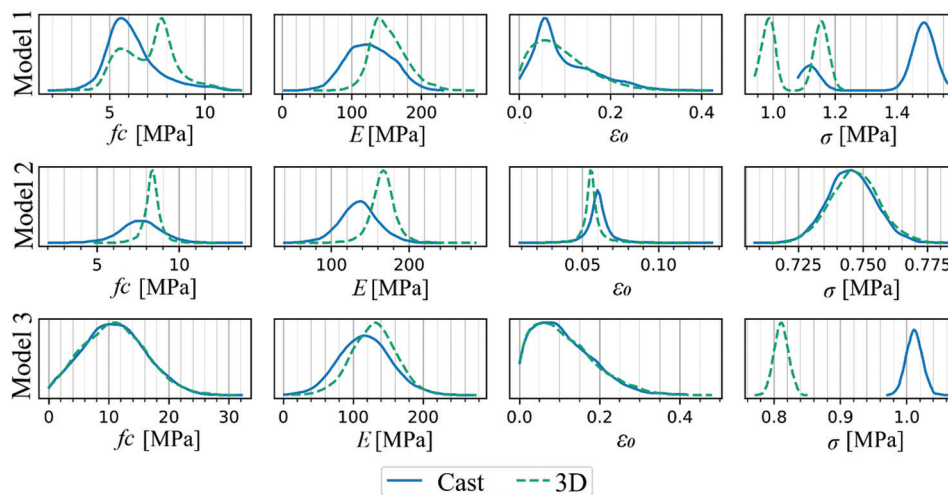


**Figure 6.** Posterior distributions for mortar parameters. Abbreviations: 3D: Three-dimensional;  $\epsilon_0$ : Peak strain;  $\sigma$ : Residual parameter;  $E$ : Elastic modulus;  $f_c$ : Compressive strength

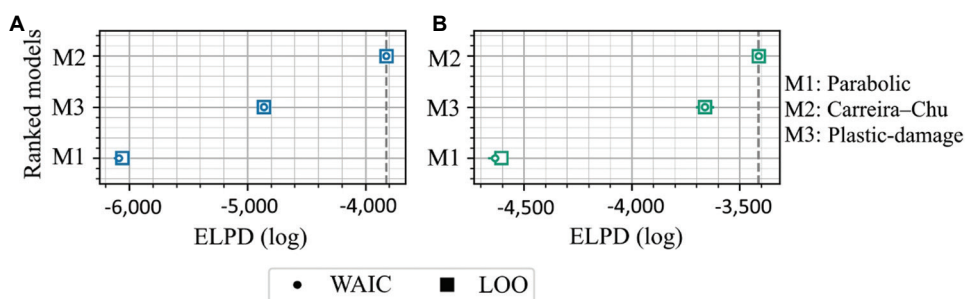


**Figure 7.** Model comparison for mortar. (A) Cast. (B) 3D-printed. Abbreviations: 3D: Three-dimensional; ELPD: Expected log predictive density; LOO: Leave-one-out; WAIC: Watanabe–Akaike Information Criterion

10.4%. The  $E$  was also higher in the printed specimens (MAP 166.8 MPa vs. 137.3 MPa). Despite these differences, the  $\sigma$  remained similar ( $\sim 0.75$  MPa), suggesting that both manufacturing methods produced results of comparable consistency. The broader HDI for  $\epsilon_0$  in printed samples reflects larger strain dispersion near peak stress, likely

related to interlayer bonding heterogeneity. In summary, the Model 2 accurately captured the stress–strain response of both cast and 3D-printed mortars, demonstrating that the 3D printing process slightly enhances strength and stiffness without altering the overall constitutive behavior of the material.

**Table 4. Comprehensive parameter estimates for mortar (Model 2)**

Parameter	Fabrication method	Mean	SD	5% HDI	95% HDI	MAP
$E$ (MPa)	Cast	135.58	24.71	95.35	177.51	137.31
	3D-printed	166.24	16.09	140.41	191.26	166.82
$\varepsilon_0$	Cast	0.060	0.008	0.049	0.073	0.0601
	3D-printed	0.056	0.007	0.048	0.067	0.0556
$f_c$ (MPa)	Cast	7.66	1.27	5.56	9.75	7.56
	3D-printed	8.36	0.54	7.53	9.18	8.35
$\sigma$ (MPa)	Cast	0.746	0.009	0.731	0.760	0.745
	3D-printed	0.747	0.009	0.732	0.763	0.746

Abbreviations: 3D: Three-dimensional;  $\varepsilon_0$ : Peak strain;  $\sigma$ : Residual parameter;  $E$ : Elastic modulus;  $f_c$ : Compressive strength; HDI: Highest density interval; MAP: Maximum a posteriori; SD: Standard deviation.

### 3.3. Three-dimensional-printed concrete

For 3D-printed concrete, posterior distributions in Figure 8 show substantial anisotropy. In OI, where the load is applied perpendicular to the printing direction, Model 2 yielded concentrated posteriors for  $E$ . In OII, where loading is parallel to the print direction, the plastic-damage model (Model 3) better captured the material response, as evidenced by broader  $\varepsilon_0$  distributions and a better fit to the experimental data.

The model selection results in Figure 9 confirm this behavior: Model 2 is optimal for OI (ELPD =  $-5,922.56 \pm 27.73$ ), while Model 3 provides the best fit for OII (ELPD =  $-5,678.27 \pm 60.10$ ).

Detailed parameter statistics in Table 5 show that the  $f_c$  was higher in OII (MAP 18.9 MPa) than in OI (MAP 16.0 MPa), representing a 18.1% increase. However, the  $E$  was substantially lower in OII (MAP 260.6 MPa) compared to OI (MAP 433.1 MPa), reflecting a stiffness–strength trade-off controlled by the printing direction.  $\sigma$  ( $\approx 1.16$  MPa) was higher in printed concrete than in the other materials, consistent with the greater heterogeneity of printed structures.

In summary, the results confirm that anisotropy plays a dominant role in the mechanical response of 3D-printed concrete. The Carreira–Chu model (Model 2) adequately represents the behavior under perpendicular loading (OI), whereas the plastic-damage model (Model 3) is required to capture the nonlinear softening and damage evolution under parallel loading (OII).

### 3.4. Summary of the Bayesian model selection results

The Bayesian model selection analysis across all material systems revealed consistent patterns linking composition,

**Table 5. Comprehensive parameter estimates for three-dimensional-printed concrete**

Parameter	Orientation	Mean	SD	5% HDI	95% HDI	MAP
$E$ (MPa)	OI (M2)	435.3	27.43	391.01	479.59	433.05
	OII (M3)	263.1	71.48	147.02	381.62	260.57
$\varepsilon_0$	OI (M2)	0.038	0.007	0.028	0.048	0.0382
	OII (M3)	0.075	0.053	0.006	0.173	0.04
$f_c$ (MPa)	OI (M2)	16.06	1.44	13.69	18.28	16.03
	OII (M3)	19.4	4.76	11.57	27.36	18.86
$\sigma$ (MPa)	OI (M2)	1.162	0.013	1.14	1.185	1.1599
	OII (M3)	1.166	0.014	1.142	1.189	1.1665

Abbreviations:  $\varepsilon_0$ : Peak strain;  $\sigma$ : Residual parameter;  $E$ : Elastic modulus;  $f_c$ : Compressive strength; HDI: Highest density interval; M2: Model 2; M3: Model 3; MAP: Maximum a posteriori; OI: Orientation I; OII: Orientation II; SD: Standard deviation.

manufacturing method, and anisotropy to the optimal constitutive model and corresponding mechanical parameters.

For the soil–cement paste, the Carreira–Chu model was selected as optimal for all  $\text{CaCO}_3$  levels, with the  $E$  decreasing from 256.9 MPa at 0%  $\text{CaCO}_3$  to 142.7 MPa at 10%, representing a 44% reduction. The  $f_c$  peaked at 4.0 MPa for 5%  $\text{CaCO}_3$ , while the  $\sigma$  declined from 0.26 MPa to 0.19 MPa, indicating improved model fit and greater response consistency despite stiffness reduction.

For the mortar with natural sand, both cast and 3D-printed specimens were best described by Model 2. 3D printing increased the  $f_c$  by approximately 9% (MAP 8.35 MPa vs. 7.56 MPa) and the  $E$  from 137.3 MPa to 166.8 MPa, with a similar  $\sigma$  (approximately 0.75 MPa). These findings confirm that additive manufacturing, under controlled deposition, can enhance densification without introducing additional variability in the mechanical response.

In the case of 3D-printed concrete, anisotropic behavior was clearly captured by the Bayesian framework. Model 2 provided the best fit for OI, while Model 3 was optimal for OII, as supported by the ELPD values ( $-5,922.6 \pm 27.7$  for OI and  $-5,678.3 \pm 60.1$  for OII). The  $E$  decreased from 433.1 MPa (OI) to 260.6 MPa (OII), while  $f_c$  increased from 16.0 MPa to 18.9 MPa, confirming a stiffness–strength trade-off governed by print orientation. The  $\sigma$  (approximately 1.16 MPa) remained consistently higher than in the paste and mortar systems, reflecting greater heterogeneity of the printed concrete.

## 4. Discussion

The Bayesian model selection process revealed how the mechanical behavior of cementitious materials is influenced by both composition and manufacturing method. Each

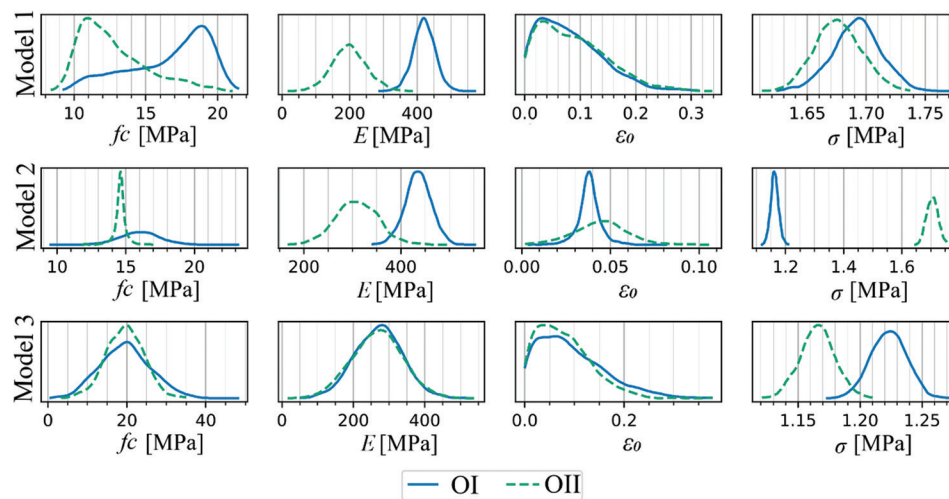


**Figure 8.** Posterior distributions for three-dimensional-printed concrete parameters

Abbreviations:  $\epsilon_o$ : Peak strain;  $\sigma$ : Residual parameter;  $E$ : Elastic modulus;  $f_c$ : Compressive strength; OI: Orientation I; OII: Orientation II

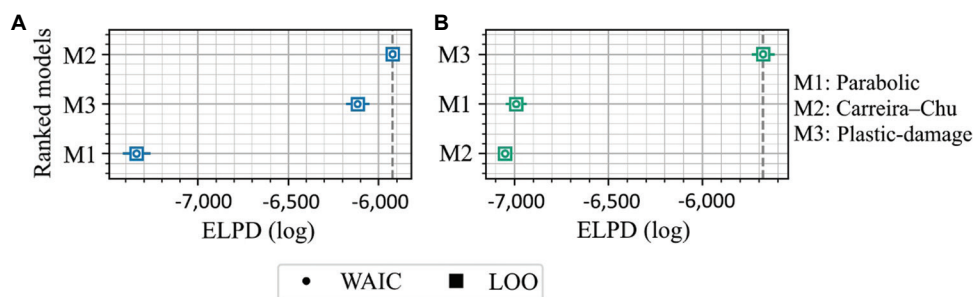


**Figure 9.** Model comparison for 3-D printed concrete. (A) Orientation I. (B) Orientation II

Abbreviations: ELPD: Expected log predictive density; LOO: Leave-one-out; WAIC: Watanabe–Akaike Information Criterion

material addressed a distinct research question: the effect of  $\text{CaCO}_3$  content in soil–cement paste, the influence of manufacturing method in mortar, and the anisotropic response of 3D-printed concrete under different loading orientations.

#### 4.1. Soil–cement paste: Effect of calcium carbonate

For soil–cement paste, the Carreira–Chu model (Model 2) was consistently selected across all  $\text{CaCO}_3$  contents, indicating that this formulation effectively captured the gradual transition from elasticity to plasticity characteristic of this material. The addition of  $\text{CaCO}_3$  reduced the  $E$  significantly (44% reduction from 0% to 10%  $\text{CaCO}_3$ ), suggesting a softening effect likely due to the disruption of the cementitious matrix. Despite this reduction in stiffness, the  $f_c$  exhibited a non-monotonic trend, increasing at 5%  $\text{CaCO}_3$  before decreasing at 10%, pointing to an optimal additive concentration that balances matrix disruption and filler effects.

The  $\sigma$  decreased with higher additive content, implying that the mechanical response became more consistent despite the reduction in stiffness. This behavior could be attributed to improved particle packing or densification at intermediate additive levels.

#### 4.2. Mortar: Manufacturing method influence

In the mortar specimens, the manufacturing method had a notable impact on mechanical properties. Both cast and printed mortars were best described by the Carreira–Chu model (Model 2), suggesting a similar constitutive form despite different fabrication techniques. The 3D-printed mortar exhibited a 9.1% higher  $f_c$  and slightly greater stiffness than the cast samples. This improvement may be associated with enhanced particle alignment and localized densification induced by the extrusion process.

However, the strain at peak stress showed broader credible intervals in the printed mortar, reflecting

greater variability in deformation mechanisms, which may be related to interlayer bonding or microstructural heterogeneities introduced during printing. Overall, these results indicate that 3D printing, under controlled conditions, does not necessarily compromise mechanical strength but introduces variability in strain localization.

### 4.3. Three-dimensional-printed concrete: Anisotropy from the printing process

The 3D-printed concrete exhibited a clear anisotropic response depending on the loading orientation. When loaded perpendicular to the print layers (OI), the Carreira–Chu model (Model 2) adequately captured the response, reflecting a gradual post-peak softening. In contrast, parallel loading (OII) required the plastic-damage model (Model 3) to reproduce the abrupt softening associated with interlayer weaknesses.

The  $f_c$  in OII orientation was 21% higher than in OI, despite a 40% lower  $E$ , confirming that stiffness is governed by layer stacking while strength is controlled by interlayer cohesion and failure mechanisms. The  $\sigma$  remained comparably high for both orientations, suggesting that anisotropy introduces heterogeneous fracture patterns regardless of loading direction.

These findings highlight that the constitutive model required to describe 3D-printed concrete is orientation-dependent, reflecting the mechanical anisotropy inherent to additive manufacturing.

### 4.4. Implications of small sample sizes and Bayesian inference

The limited number of specimens tested for each material—four for each  $\text{CaCO}_3$  content in paste, and two to three for mortar and concrete—introduces uncertainty in the parameter estimates. Bayesian inference mitigates this limitation by providing full probability distributions rather than relying solely on point estimates, allowing uncertainty to be explicitly quantified through the HDI and the  $\sigma$ .

In the mortar results, the small sample size may partially explain the apparent increase in strength of the printed specimens. Although printing may improve densification, limited replication can amplify observed differences between fabrication methods. These observations underscore the importance of Bayesian approaches in experimental contexts with small datasets, where probabilistic inference enhances result robustness and interpretability.

### 4.5. General observations on model selection

The results show that the Carreira–Chu model (Model 2) adequately represented the mechanical response in several cases: soil–cement paste at all additive contents, both

fabrication methods in mortar, and 3D-printed concrete loaded perpendicular to the print layers (OI). In these cases, the stress–strain behavior exhibited a gradual elastic–plastic transition, which this model effectively captured, regardless of potential microstructural heterogeneities.

In contrast, the plastic-damage model (Model 3) was required for 3D-printed concrete under parallel loading, where the abrupt post-peak softening and damage evolution were direction-dependent. These findings confirm that Bayesian model selection not only identifies the most appropriate constitutive formulation but also clarifies how different material compositions and manufacturing processes influence stiffness, strength, and post-peak behavior.

## 5. Conclusion

This study employed a hierarchical Bayesian framework to calibrate and select constitutive models for cementitious materials produced through additive manufacturing and conventional casting. The probabilistic formulation enables robust model selection and uncertainty quantification, even for small experimental datasets. The key findings are as follows:

- (i) Material composition effects: In soil–cement pastes, the inclusion of  $\text{CaCO}_3$  progressively reduced stiffness while moderately enhancing  $f_c$  at intermediate concentrations. The Carreira–Chu model (Model 2) effectively captured this smooth elastic–plastic transition.
- (ii) Manufacturing process influence: For mortars, 3D-printed specimens showed slightly higher  $f_c$  than cast counterparts, reflecting enhanced densification during deposition. Both fabrication methods exhibited similar constitutive behavior represented by Model 2.
- (iii) Anisotropy in 3D-printed concrete: Directional testing confirmed the anisotropic mechanical behavior induced by layer-by-layer deposition. Perpendicular loading (OI) was well described by Model 2, while parallel loading (OII) required the plastic-damage model (Model 3) to reproduce the abrupt post-peak softening associated with interlayer weaknesses.
- (iv) Methodological contribution: The hierarchical Bayesian approach provides population- and specimen-level parameter estimation with credible uncertainty ranges (HDI,  $\sigma$ ). This framework enhances the interpretability of mechanical characterization in additively manufactured materials.

Overall, the proposed framework bridges experimental data and probabilistic modeling, offering a reliable tool for constitutive model selection in additive construction materials. Future work will extend this methodology to tensile and flexural behavior and evaluate the influence of printing parameters—such as layer orientation, extrusion

rate, and interlayer time—on the mechanical response. This will enable a deeper understanding of how process variables affect anisotropy and structural performance in 3D-printed concrete.

## Acknowledgments

The authors acknowledge Nathalia Conde-Cacedo, Ruby Mejía de Gutiérrez, and Rafael Robayo-Salazar from the Composites Materials Group (GMC-CENM) for providing part of the experimental data used in this study, generated within the research project supporting this work.

## Funding

This research was supported by the Ministry of Science, Technology, and Innovation, Colombia, through Funding Call 6 of the 2021–2022 biennium of the General Royalties System, within the framework of the project “Development of a 3D printing system of sustainable non-conventional materials for the advancement of rural infrastructure in the department of Cauca” (BPIN 2020000100625) at Universidad del Valle.

## Conflict of interest

The authors declare that there are no conflicts of interest regarding the publication of this paper.

## Author contributions

*Conceptualization:* Albert R. Ortiz, Peter Thomson

*Formal analysis:* Felipe Guerrero, Albert R. Ortiz

*Funding acquisition:* Daniel Gomez

*Investigation:* Felipe Guerrero, Albert R. Ortiz

*Methodology:* Albert R. Ortiz, Felipe Guerrero

*Supervision:* Daniel Gomez

*Writing—original draft:* Felipe Guerrero

*Writing—review & editing:* All authors

## Ethics approval and consent to participate

Not applicable.

## Consent for publication

Not applicable.

## Availability of data

The datasets generated and analyzed during the current study are available from the corresponding author upon reasonable request.

## References

1. Mechtcherine V, Bos FP, Perrot A, *et al.* Extrusion-based additive manufacturing with cement-based materials - production steps, processes, and their underlying physics: A review. *Cem Concr Res.* 2020;132:106037. doi: 10.1016/j.cemconres.2020.106037
2. Mechtcherine V, Nerella VN, Will F, Näther M, Otto J, Krause M. Large-scale digital concrete construction - CONPrint3D concept for on-site, monolithic 3D-printing. *Autom Constr.* 2019;107:102933. doi: 10.1016/j.autcon.2019.102933
3. Shakor P, Nejadi S, Sutjipto S, Paul G, Gowripalan N. Effects of deposition velocity in the presence/absence of E6-glass fibre on extrusion-based 3D printed mortar. *Addit Manuf.* 2020;32:101069. doi: 10.1016/j.addma.2020.101069
4. Van Zijl GP, Paul SC, Tan MJ. *Properties of 3D Printable Concrete. Paper Presented at: 2<sup>nd</sup> International Conference on Progress in Additive Manufacturing (Pro-AM 2016);* May 16-19. Nanyang, Singapore; 2016. Available from: <https://www.com/url: hdl.handle.net/10356/84556> [Last accessed on 2026 Mar 04].
5. Li M, Weng Y, Liu Z, Zhang D, Wong TN. Optimizing of chemical admixtures for 3D printable cementitious materials by central composite design. *Mater Sci Addit Manuf.* 2022;1(3):16. doi: 10.18063/msam.v1i3.16
6. Roussel N, Bessaies-Bey H, Kawashima S, Marchon D, Vasilic K, Wolfs R. Recent advances on yield stress and elasticity of fresh cement-based materials. *Cem Concr Res.* 2019;124:105798. doi: 10.1016/j.cemconres.2019.105798
7. Mader T, Schreter-Fleischhacker M, Shkundalova O, Neuner M, Hofstetter G. Constitutive modeling of orthotropic nonlinear mechanical behavior of hardened 3D printed concrete. *Acta Mech.* 2023;234(11):5893-5918. doi: 10.1007/s00707-023-03706-z
8. Robayo-Salazar R, Martínez F, Vargas A, Mejía De Gutiérrez R. 3D printing of hybrid cements based on high contents of powders from concrete, ceramic and brick waste chemically activated with sodium sulphate (Na<sub>2</sub>SO<sub>4</sub>). *Sustainability.* 2023;15(13):9900. doi: 10.3390/su15139900
9. Tay YWD, Panda B, Paul SC, Mohamed NAN, Tan MJ, Leong KF. 3D printing trends in building and construction industry: A review. *Virtual Phys Prototyp.* 2017;12(3):261-276. doi: 10.1080/17452759.2017.1326724
10. Paolini A, Kollmannsberger S, Rank E. Additive manufacturing in construction: A review on processes, applications, and digital planning methods. *Addit Manuf.* 2019;30:100894. doi: 10.1016/j.addma.2019.100894
11. Paul SC, Tay YWD, Panda B, Tan MJ. Fresh and hardened properties of 3D printable cementitious materials for building and construction. *Arch Civ Mech Eng.* 2018;18(1):311-319.

- doi: 10.1016/j.acme.2017.02.008
12. Ding T, Xiao J, Zou S, Wang Y. Hardened properties of layered 3D printed concrete with recycled sand. *Cem Concr Compos.* 2020;113:103724.  
doi: 10.1016/j.cemconcomp.2020.103724
13. Kaliyavaradhan SK, Ambily PS, Prem PR, Ghodke SB. Test methods for 3D printable concrete. *Autom Constr.* 2022;142:104529.  
doi: 10.1016/j.autcon.2022.104529
14. Chougan M, Ghaffar SH, Sikora P, *et al.* Investigation of additive incorporation on rheological, microstructural and mechanical properties of 3D printable alkali-activated materials. *Mater Des.* 2021;202:109574.  
doi: 10.1016/j.matdes.2021.109574
15. Kruger J, Van Der Westhuizen JP. Investigating the poisson ratio of 3D printed concrete. *Appl Sci.* 2023;13(5):3225.  
doi: 10.3390/app13053225
16. Le TT, Austin SA, Lim S, *et al.* Hardened properties of high-performance printing concrete. *Cem Concr Res.* 2012;42(3):558-566.  
doi: 10.1016/j.cemconres.2011.12.003
17. Feng P, Meng X, Chen JF, Ye L. Mechanical properties of structures 3D printed with cementitious powders. *Constr Build Mater.* 2015;93:486-497.  
doi: 10.1016/j.conbuildmat.2015.05.132
18. Riaz RD, Usman M, Ali A, Majid U, Faizan M, Malik UJ. Inclusive characterization of 3D printed concrete (3DPC) in additive manufacturing: A detailed review. *Constr Build Mater.* 2023;394:132229.  
doi: 10.1016/j.conbuildmat.2023.132229
19. Rahul AV, Santhanam M, Meena H, Ghani Z. Mechanical characterization of 3D printable concrete. *Constr Build Mater.* 2019;227:116710.  
doi: 10.1016/j.conbuildmat.2019.116710
20. Soltan DG, Li VC. A self-reinforced cementitious composite for building-scale 3D printing. *Cem Concr Compos.* 2018;90:1-13.  
doi: 10.1016/j.cemconcomp.2018.03.017
21. Pham L, Tran P, Sanjayan J. Steel fibres reinforced 3D printed concrete: Influence of fibre sizes on mechanical performance. *Constr Build Mater.* 2020;250:118785.  
doi: 10.1016/j.conbuildmat.2020.118785
22. Ding T, Xiao J, Zou S, Zhou X. Anisotropic behavior in bending of 3D printed concrete reinforced with fibers. *Compos Struct.* 2020;254:112808.  
doi: 10.1016/j.compstruct.2020.112808
23. Reinold J, Nerella VN, Mechtcherine V, Meschke G. Extrusion process simulation and layer shape prediction during 3D-concrete-printing using the particle finite element method. *Autom Constr.* 2022;136:104173.  
doi: 10.1016/j.autcon.2022.104173
24. Papanastasiou TC. Flows of materials with yield. *J Rheol.* 1987;31(5):385-404.  
doi: 10.1122/1.549926
25. Liu C, Wang Z, Wu Y, *et al.* 3D printing concrete with recycled sand: The influence mechanism of extruded pore defects on constitutive relationship. *J Build Eng.* 2023;68:106169.  
doi: 10.1016/j.job.2023.106169
26. Xiao J, Li J, Zhang C. Mechanical properties of recycled aggregate concrete under uniaxial loading. *Cem Concr Res.* 2005;35(6):1187-1194.  
doi: 10.1016/j.cemconres.2004.09.020
27. Grassl P, Jirásek M. Damage-plastic model for concrete failure. *Int J Solids Struct.* 2006;43(22-23):7166-7196.  
doi: 10.1016/j.ijsolstr.2006.06.032
28. Carreira DJ, Chu KH. Stress-strain relationship for plain concrete in compression. *ACI J Proc.* 1985;82(6):797-804.  
doi: 10.14359/10390
29. Ouyang X, Wu Z, Shan B, Chen Q, Shi C. A critical review on compressive behavior and empirical constitutive models of concrete. *Constr Build Mater.* 2022;323:126572.  
doi: 10.1016/j.conbuildmat.2022.126572
30. Saenz LP. Discussion of "equation for the stress-strain curve of concrete" by Desayi and Krishnan. *J Am Concr Inst.* 1964;61:1229-1235.
31. Xiao J, Liu H, Ding T. Finite element analysis on the anisotropic behavior of 3D printed concrete under compression and flexure. *Addit Manuf.* 2021;39:101712.  
doi: 10.1016/j.addma.2020.101712
32. Hordijk DA. *Local Approach to Fatigue of Concrete*. Delft University of Technology [Dissertation]; 1991.
33. Watanabe S. WAIC and WBIC are Information Criteria for Singular Statistical Model Evaluation. In: *Proceedings of the Workshop on Information Theoretic Methods in Science and Engineering*. 2013. p. 90-94.
34. Vehtari A, Gelman A, Gabry J. Practical Bayesian model evaluation using leave-one-out cross-validation and WAIC. *Stat Comput.* 2017;27(5):1413-1432.  
doi: 10.1007/s11222-016-9696-4
35. Abril-Pla O, Andreani V, Carroll C, *et al.* PyMC: A modern, and comprehensive probabilistic programming framework in Python. *PeerJ Comput Sci.* 2023;9:e1516.  
doi: 10.7717/peerj-cs.1516
36. Gelman A, Carlin JB, Stern HS, Dunson DB, Vehtari A, Rubin DB. *Bayesian Data Analysis*. United States: CRC Press; 2013.
37. Gelman A, Rubin DB. Inference from iterative simulation using multiple sequences. *Stat Sci.* 1992;7(4):457-472.